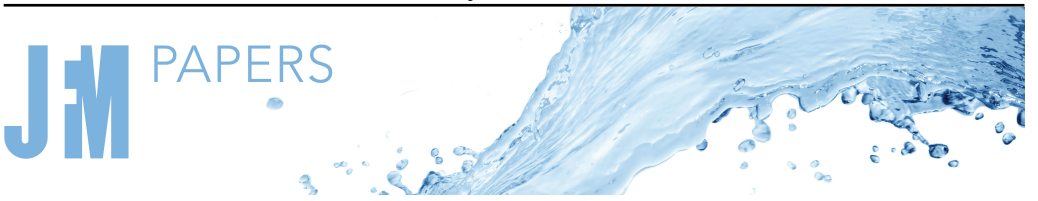
J. Fluid Mech. (2026), *vol.* 1046, A64, doi:10.1017/jfm.2026.12243



Interfacial transitions in vibrated immiscible two-phase flow under microgravity

Chao-Ben Zhao[1], **Cheng Tian**[1], **Kai Leong Chong**[2], **Quan Zhou**[2] and **Chao Sun**[1,3]

[1]New Cornerstone Science Laboratory, Center for Combustion Energy, Key Laboratory for Thermal Science and Power Engineering of Ministry of Education, Department of Energy and Power Engineering, Tsinghua University, Beijing 100084, PR China

[2]Shanghai Key Laboratory of Mechanics in Energy Engineering, Shanghai Institute of Applied Mathematics and Mechanics, School of Mechanics and Engineering Science, Shanghai University, Shanghai 200072, PR China

[3]Department of Engineering Mechanics, School of Aerospace Engineering, Tsinghua University, Beijing 100084, PR China

Corresponding authors: Kai Leong Chong, klchong@shu.edu.cn; Quan Zhou, qzhou@shu.edu.cn; Chao Sun, chaosun@tsinghua.edu.cn

(Received 24 May 2026 UTC; revised 25 September 2026 UTC; accepted 25 September 2026 UTC)

We investigate how vibration-driven interfacial state transitions regulate heat transport in an immiscible two-phase layer under microgravity. Direct numerical simulations are performed for two immiscible fluid layers subject to a vertical temperature difference and horizontal harmonic vibration, while the Weber number and thermal-expansion contrast are varied systematically. As the Weber number increases, the dispersed phase evolves from a stratified-layer state to an interfacial-bulging state and then to a droplet-dispersed state, and the global Nusselt and Reynolds numbers accordingly separate into three regimes. We identify two critical thresholds associated with the onset of interfacial bulging and droplet detachment; both move to lower Weber number as the thermal-expansion contrast increases. The first threshold is set by the pressure balance between thermovibrational pressure difference and capillary restoring stress, and the second threshold is set by the force balance between the thermovibrational force acting on the lifted liquid volume and the capillary force retaining the remaining neck. When rescaled by the corresponding critical thresholds, the onset of the bulging and detachment transitions collapses across different thermal-expansion contrasts, together with the associated changes in the Nusselt and Reynolds numbers. Our results show that interfacial

© The Author(s), 2026. Published by Cambridge University Press.

https://doi.org/10.1017/jfm.2026.12243

morphology provides the key link between vibration forcing and transport response, and establishes a compact regime-based framework for regulating microgravity two-phase heat transport.

Key words: multiphase flow, interfacial flows

1. Introduction

Fluid motion and transport in microgravity are of both fundamental and practical relevance to space thermal management, materials processing, and phase-change technologies. Under terrestrial conditions, gravity provides a natural route for generating buoyancy-driven flow and thereby regulating transport. The canonical example is Rayleigh–Bénard convection, which has long served as a benchmark system for studying thermal turbulence, heat transport, boundary layers and coherent flow organisation (Siggia 1994; Ahlers *et al.* 2009; Lohse & Xia 2010; Chillà & Schumacher 2012; Lohse & Shishkina 2023, 2024; Xia *et al.* 2023, 2025).

In microgravity, by contrast, this mechanism is strongly attenuated, so alternative means of driving fluid motion are required. Mechanical vibration provides a promising alternative, because it is ubiquitous in reduced-gravity environments and can create an effective 'artificial gravity' that drives fluid motion and modifies transport processes (Gershuni & Lyubimov 1998; Beysens *et al.* 2005; Beysens 2006; Lappa 2009; Guo *et al.* 2023; Huang *et al.* 2024). Correspondingly, theoretical and experimental studies have established vibroconvection as a viable mechanism of heat and mass transport in low-gravity conditions (Mialdun *et al.* 2008; Shevtsova *et al.* 2010). However, many low-gravity transport processes involve multiple fluid phases, for which the response to vibration can depend sensitively on phase arrangement and interfacial coupling. These considerations motivate the study of vibroconvection in immiscible two-phase systems, where a deformable interface couples capillarity, phase connectivity and external forcing to the transport process.

Previous studies have established that vibration can substantially alter thermally driven flow. Classical analyses and numerical studies showed that vibration can change convective structures and transport in enclosed fluids under weightless or high-frequency forcing conditions (Gershuni *et al.* 1982; Savino *et al.* 1998; Hirata *et al.* 2001; Cisse *et al.* 2004). More recent work has shown that the effect of vibration is not restricted to modulating flow intensity: it can reorganise thermal boundary layers, alter large-scale flow structures and induce distinct transport regimes in thermal convection (Wang *et al.* 2020*a*; Guo *et al.* 2023; Huang *et al.* 2023, 2024). Externally forced multiphase systems have likewise been found to exhibit diverse interfacial dynamics, including forcing-dependent symmetry breaking and multiple interfacial states of bubbles (Guan *et al.* 2025). These studies indicate that, once a deformable interface is present, the response to vibration is governed not only by bulk convection but also by forcing-selected interfacial states, reflecting a competition between flow reorganisation and interfacial dynamics.

In thermally driven two-phase flows, interfacial physics is central even in the absence of vibration, and the motion of drops and bubbles across sharp interfaces or stratified layers is known to be strongly shaped by interfacial deformation and capillarity (Magnaudet & Mercier 2020). Early studies of layered thermal convection examined thermal coupling and natural convection in multiple layers of immiscible liquids (Nataf *et al.* 1988; Prakash & Koster 1994), while later experiments addressed turbulent two-layer convection and the coupling between the large-scale circulations across the interface (Xie & Xia 2013). This

https://doi.org/10.1017/jfm.2026.12243

two-layer turbulent-convection picture has further motivated reduced-order modelling of the coupled large-scale circulations and their reversals (Sun *et al.* 2024). Recent experiments on thermal convection with two liquid layers and three-layer turbulent thermal convection have further shown that heat transport and flow organisation are strongly affected by the layered configuration and interfacial coupling (Wang *et al.* 2024; Zhao *et al.* 2024). More recent numerical work showed that interface breakup can arise in two-layer thermally driven turbulence (Liu *et al.* 2021*a*), that immiscible interfaces can exert a strong influence on transport in layered convection (Liu *et al.* 2022*b*), and that global transport may depend only weakly on *We* even though interface fluctuations and interfacial-wave dynamics remain sensitive to it over the Rayleigh–Weber parameter space (Demou *et al.* 2024). In liquid–liquid dispersions, interfacial stabilisation has been shown to control morphology and convective heat-transfer dynamics (Pelusi *et al.* 2025*b*), while thermally convective emulsions may develop distinct regimes associated with breakup, coalescence and phase inversion (Pelusi *et al.* 2025*a*).

The organising role of interfaces is also evident in emulsions and other dispersed flows. Interfacial deformation, breakup, coalescence and phase inversion control droplet statistics and bulk transport (Perlekar *et al.* 2012; Perazzo *et al.* 2015; Mukherjee *et al.* 2019; Soligo *et al.* 2019; Bakhuis *et al.* 2021; Yi *et al.* 2021, 2022, 2023, 2024; Ravera *et al.* 2021; Ni 2024; Sun & Toschi 2027), while dispersed droplets can modify drag and interfacial transport in wall-bounded and shear-driven flows (Rosti *et al.* 2019; Hori *et al.* 2023; Su *et al.* 2024*a*, 2024*b*, 2025; Fan *et al.* 2025). Related changes in heat transfer and flow fluctuations occur in thermally driven multiphase systems (Wang *et al.* 2019, 2020*b*; Liu *et al.* 2021*a*,*b*, 2022*a*; Qi *et al.* 2026; Meng *et al.* 2026; Pelusi *et al.* 2021) and in bubbly or particle-laden flows (Lakkaraju *et al.* 2011; Mathai *et al.* 2020; Liu *et al.* 2022*c*). Applications such as inkjet printing likewise underscore the importance of deformation and pinch-off (Lohse 2022). These studies suggest that interfacial deformation and loss of phase connectivity can reorganise transport in vibrated immiscible systems under microgravity.

Vibration-driven immiscible two-phase flow under microgravity can therefore be viewed as a problem in which transport is controlled by the interfacial states selected by the competition between vibration and capillarity. The forcing strength and material contrast are expected to jointly determine the interfacial morphology, while transitions between different interfacial states should, in turn, reorganise the global flow and transport responses. To this end, we carry out direct numerical simulations of an immiscible two-phase layer subjected to a vertical temperature difference and horizontal harmonic vibration under microgravity conditions. We show that the competition between vibration, capillarity and material contrast leads to three interfacial states, and that two critical Weber numbers collapse the corresponding regime transitions. The remainder of the paper is organised as follows. The numerical method is introduced in § 2. The flow morphology, transport responses and regime transitions are presented in § 3. Finally, the main findings are summarised in § 4.

2. Numerical methods

We consider thermally coupled immiscible two-phase flow in a microgravity cell. The thermally coupled two-layer configuration follows the general set-up studied by Liu *et al.* (2022*b*). The two-dimensional computational domain is a rectangle of width $2H$ and height H, namely $x \in [-H, H]$ and $z \in [-H/2, H/2]$. Additional three-dimensional calculations are performed in a cuboidal domain with dimensions $L_x \times L_y \times L_z = 2H \times H \times H$, where z is the vertical direction. A constant temperature difference Δ is imposed

https://doi.org/10.1017/jfm.2026.12243

in the vertical direction, with the top wall maintained at $-\Delta/2$ and the bottom wall at $\Delta/2$. Since the present study concerns the microgravity regime, steady gravitational buoyancy is omitted and a horizontal harmonic vibration $A\cos(\Omega t)\hat{\boldsymbol{e}}_x$ is imposed to act as an artificial driving. In the non-inertial frame associated with the imposed vibration, an inertial acceleration in the horizontal direction is introduced into the system, thereby generating vibroconvection (Gershuni & Lyubimov 1998; Shevtsova *et al.* 2010; Huang *et al.* 2024). Here, A and Ω denote the dimensional vibration amplitude and angular frequency, respectively, and $\hat{\boldsymbol{e}}_x$ is the unit vector in the horizontal direction. We employ a one-fluid description to simulate the immiscible two-phase system, in which the two fluids are distinguished by a phase indicator C, with $C=0$ in fluid 0 and $C=1$ in fluid 1. The treatment of thermally coupled multiphase transport follows in the spirit of Liu *et al.* (2021*b*, 2022*b*). All quantities are made dimensionless with respect to the cell height H, the imposed temperature difference Δ, the vibration-induced velocity scale $U_v=\alpha_0 A\Omega\Delta$, the time scale H/U_v and the pressure scale $\rho_0 U_v^2$. In this scaling, α_0 denotes the reference thermal-expansion coefficient of fluid 0. The resulting non-dimensional governing equations for this system read

$$\nabla\cdot\boldsymbol{u}=0, \tag{2.1}$$

$$\tilde{\rho}\,(\partial_t\boldsymbol{u}+\boldsymbol{u}\cdot\nabla\boldsymbol{u})=-\nabla p+\sqrt{\frac{Pr}{2Ra_{vib}}}\nabla\cdot\left[\tilde{\mu}\left(\nabla\boldsymbol{u}+\nabla\boldsymbol{u}^T\right)\right]+\boldsymbol{F}_{st}+\boldsymbol{G}_{vib}, \tag{2.2}$$

$$\tilde{\rho}\tilde{c}_p\,(\partial_t\theta+\boldsymbol{u}\cdot\nabla\theta)=\frac{1}{\sqrt{2PrRa_{vib}}}\nabla\cdot\left(\tilde{k}\nabla\theta\right), \tag{2.3}$$

$$\partial_t C+\boldsymbol{u}\cdot\nabla C=0. \tag{2.4}$$

Here, the capillary force is written as

$$\boldsymbol{F}_{st}=\frac{1}{We}\kappa\delta_s\hat{\boldsymbol{n}}, \tag{2.5}$$

where $\hat{\boldsymbol{n}}=\nabla C/|\nabla C|$ is the unit normal directed from fluid 0 to fluid 1, $\kappa=-\nabla\cdot\hat{\boldsymbol{n}}$ is the interfacial curvature and $\delta_s=|\nabla C|$ is the surface delta distribution in the continuum-surface-force representation, while the vibration forcing is

$$\boldsymbol{G}_{vib}=a^{-1}\tilde{\rho}\tilde{\alpha}\,\theta\,\cos\left(a^{-1}t\right)\hat{\boldsymbol{e}}_x. \tag{2.6}$$

Here, $\boldsymbol{u}$ is the dimensionless velocity field, p is the dimensionless pressure and θ is the dimensionless temperature. The capillary contribution is represented by $\boldsymbol{F}_{st}$ and the vibrational forcing by $\boldsymbol{G}_{vib}$. Surface tension is assumed to be temperature-independent, so thermocapillary (Marangoni) stresses are neglected. This isolates the competition between thermovibrational forcing and capillary restoration, and the results apply most directly when thermocapillary effects are weak. To assess this approximation, we use H as the characteristic tangential length and compare the thermocapillary stress $|\mathrm{d}\sigma/\mathrm{d}T|\Delta T_\parallel/H$ with the reference thermovibrational inertial stress $\rho_0 U_v^2$, defining

$$\Pi_M=\frac{|\mathrm{d}\sigma/\mathrm{d}T|\,\Delta T_\parallel}{\rho_0 U_v^2 H}=\frac{|\mathrm{d}\sigma/\mathrm{d}T|\,\Delta T_\parallel H}{2\rho_0 Ra_{vib}\nu_0\kappa_0}. \tag{2.7}$$

Here, $\Delta T_\parallel$ is the dimensional temperature variation along the interface, distinct from the imposed wall-temperature difference Δ. Thus, $\Pi_M\ll 1$ indicates a weak thermocapillary contribution on the cell scale. Water–silicone oil (Peters & Arabali 2013) and 20 cSt silicone oil–Fluorinert (Someya & Munakata 2005) are examples of immiscible fluid

https://doi.org/10.1017/jfm.2026.12243

pairs studied experimentally. Taking these systems as examples, we make illustrative estimates using representative reference-fluid properties and assumed interfacial-tension temperature coefficients. For $Ra_{vib} = 10^5$ and $H = 10$ cm, we obtain $\Pi_M/\Delta T_\parallel \approx 0.50$ and 6.6×10^{-3} K^{-1}, respectively, using water and silicone oil as the reference fluids. The latter estimate remains small for interfacial temperature variations of several Kelvin, whereas the former requires much smaller variations. These order-of-magnitude estimates illustrate the approximation's scope; the simulations use idealised material properties rather than those of either of the experimental fluid pair, with only the thermal-expansion coefficients differing between phases. Finite Marangoni forcing may modify the interfacial dynamics, transition thresholds and heat transport.

All dimensionless material properties, denoted by $\tilde{q}$, are defined uniformly as

$$\tilde{q} = C\lambda_q + (1 - C), \tag{2.8}$$

where $\lambda_q = q_1/q_0$ is the ratio of the material property q in fluid 1 to the reference value q_0, with $q \in \{\rho, \mu, k, c_p, \alpha\}$. The dimensionless vibration amplitude is $a = \alpha_0 A\Delta/H$, so that the dimensionless forcing frequency under the present velocity scale is $\omega \equiv \Omega H/U_v = a^{-1}$. The principal dimensionless control parameters are

$$a = \frac{\alpha_0 A\Delta}{H}, \qquad Ra_{vib} = \frac{(\alpha_0 A\Omega\Delta H)^2}{2\nu_0\kappa_0}, \tag{2.9}$$

$$Pr = \frac{\nu_0}{\kappa_0}, \qquad We = \frac{\rho_0(\alpha_0 A\Omega\Delta)^2 H}{\sigma}, \tag{2.10}$$

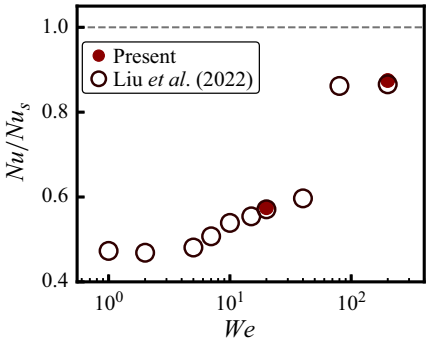
where A and Ω denote the dimensional vibration amplitude and angular frequency, respectively. In what follows, the thermal-expansion contrast is denoted by α_1/α_0. Unlike the classical Rayleigh number governing gravitational convection, $Ra_{vib} = U_v^2 H^2/(2\nu_0\kappa_0)$ measures thermovibrational forcing relative to viscous and thermal diffusion. In the high-frequency limit, it characterises the induced mean flow (Gershuni & Lyubimov 1998; Lappa 2009), while ω, or equivalently $a = \omega^{-1}$ under the present scaling, remains an independent parameter governing the temporal response. For the main parameter sweep, we fix $Ra_{vib} = 10^5$, $Pr = 4.38$ and $a = 0.01$, vary We over $0.1 \leqslant We \leqslant 3000$, and consider $\alpha_1/\alpha_0 = 3, 4, 5, 6, 7$. All other material-property ratios are unity.

The governing equations are solved numerically using an in-house code developed based on the open-source Basilisk C framework (Popinet 2013). The incompressible Navier–Stokes equations are advanced with the centred projection method, while the interface is captured with the geometrical volume-of-fluid method and the balanced-force treatment of surface tension (Popinet 2009, 2015). The temperature field is treated as a conservative scalar with variable volumetric heat capacity and thermal conductivity. The coupled two-phase implementation is benchmarked against the two-layer thermal-convection results of Liu *et al.* (2022*b*) (figure 1). The normalised Nusselt numbers at $We = 20$ and 200 differ from the reference values by 0.67 % and 1.04 %, respectively, while the $We = 20$ temperature field reproduces the reported interfacial deformation and thermal structure. Additional tests of thermovibrational forcing, stationary two-layer conduction and interface capturing during breakup are reported in Appendix A.

Second, we suppress motion and vibration, and consider stationary conduction through two equal-depth immiscible layers, $H_0 = H_1 = H/2$. With all property ratios except $\lambda_k = k_1/k_0$ set to unity, we test $\lambda_k = 0.5$, 1, 2 and 5. For the boundary conditions, the top and bottom plates at $z = \pm H/2$ are rigid no-slip walls. The lateral boundaries are periodic: in the two-dimensional simulations, this applies to the x direction, whereas in the three-dimensional simulations, both the x and y directions are periodic. In the

https://doi.org/10.1017/jfm.2026.12243

(*a*)



(*b*)

We	Present Nu/Nu_s	Liu *et al.* Nu/Nu_s	Difference (%)
20	0.5748	0.5710	0.67
200	0.8746	0.8657	1.04

(*c*) Present (*d*) Liu *et al.* (2022)

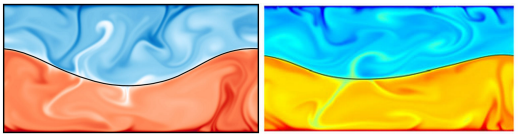


Figure 1. Validation against the two-layer thermal-convection results of Liu *et al.* (2022*b*). (*a*) Nusselt number normalised by the corresponding single-phase value, Nu/Nu_s, as a function of *We*. (*b*) Present values and their relative differences from the reference data at $We = 20$ and 200. Instantaneous temperature fields at $We = 20$ from (*c*) the present simulation and (*d*) Liu *et al.* (2022*b*). The black contour in panel (*c*) denotes the liquid–liquid interface at $C = 0.5$.

present non-dimensionalisation, the wall temperatures are fixed at $\theta = -1/2$ on the top wall and $\theta = 1/2$ on the bottom wall. For the initial condition, the flow is initialised from a quiescent two-layer configuration. In two dimensions, the initial interface is prescribed through the phase indicator as

$$C(x, z, 0) = \mathcal{H}(H_{layer} - z), \tag{2.11}$$

with the analogous three-dimensional initialisation $C(x, y, z, 0) = \mathcal{H}(H_{layer} - z)$. Here, $\mathcal{H}(\cdot)$ is the Heaviside function and H_{layer} determines the initial layer height. The dispersed phase is initially placed in the lower layer with a fixed volume fraction

$$\phi_d = \frac{1}{|\mathcal{D}|} \int_{\mathcal{D}} C(\boldsymbol{x}, 0)\, \mathrm{d}\mathcal{D} = 0.2, \tag{2.12}$$

where $\mathcal{D}$ denotes the computational domain, with $\mathrm{d}\mathcal{D}$ representing an area element in two dimensions and a volume element in three dimensions. Since the dimensionless cell height is unity, this corresponds to $H_{layer} = -0.3$ in the domain $z \in [-1/2, 1/2]$; the resulting 20 % dispersed-phase loading is comparable to the minority-layer fractions considered in previous two-layer thermal-convection simulations (Liu *et al.* 2022*b*). The initial temperature field is taken to be a linear conductive profile plus a small random perturbation,

$$\theta(x, z, 0) = -z + \epsilon\, \xi(x, z), \tag{2.13}$$

with the corresponding three-dimensional form $\theta(x, y, z, 0) = -z + \epsilon\, \xi(x, y, z)$. Here, ξ is a zero-mean random field and ϵ is a small perturbation amplitude. The initial velocity field is set to $\boldsymbol{u} = 0$.

For spatial discretisation, the parameter-sweep simulations use a uniform 512×256 grid for all fields. Within the Basilisk multigrid framework, the three-dimensional validation cases use a $256 \times 128 \times 128$ grid for velocity, pressure and temperature, and a $512 \times 256 \times 256$ grid for the VOF field. Grid-refinement tests based on M_{det}, *Nu* and *Re* support the adequacy of the production grid (Appendix B). The time step is adjusted dynamically from the CFL restriction; for low-*We* cases, a smaller CFL cap is used to improve robustness. In addition, a smooth start-up factor is applied in low-*We* cases to avoid spurious initial transients. Statistics are accumulated only after the flow reaches

https://doi.org/10.1017/jfm.2026.12243

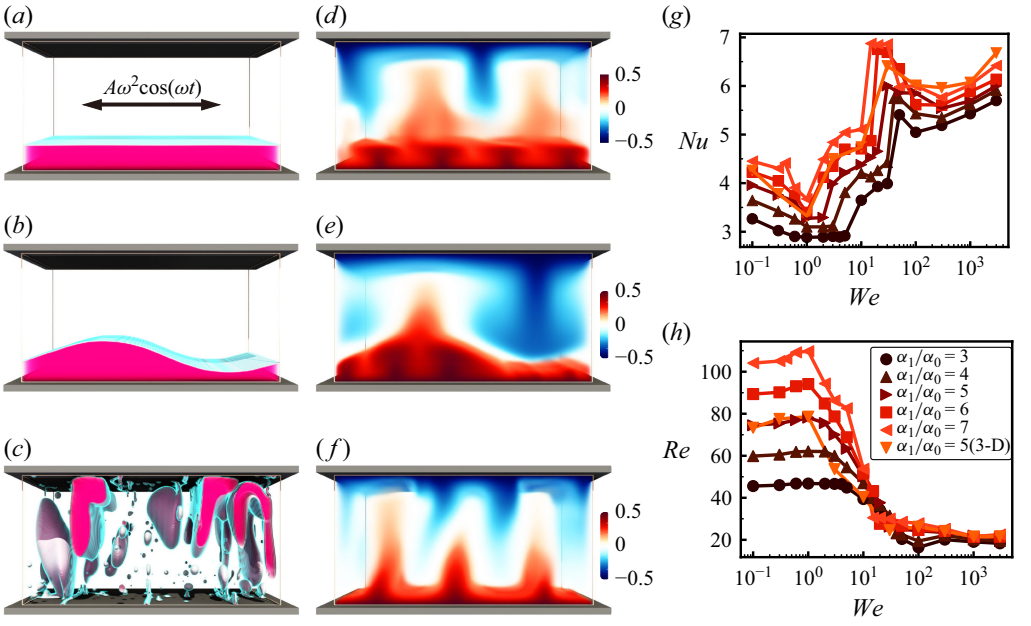


Figure 2. (*a*)–(*c*) Three-dimensional visualisations of the dispersed-phase morphology at Weber numbers (*a*) $We = 0.1$, (*b*) $We = 2$ and (*c*) $We = 1000$. The panels show the transition from a stratified-layer state to an interfacial-bulging state and then to a droplet-dispersed state. (*d*)–(*f*) Corresponding three-dimensional temperature fields for the same three Weber numbers, showing the accompanying reorganisation of the thermal structure. (*g*) Nusselt number Nu as a function of We for different thermal-expansion contrasts α_1/α_0 from the two-dimensional parameter sweep, together with representative three-dimensional results. (*h*) Reynolds number Re as a function of We for the same cases. All cases are performed at fixed $Ra_{vib} = 10^5$ and vibration amplitude $a = 0.01$.

a statistically stationary state and span at least 600 dimensionless time units, with time scaled by H/U_v. We assess convergence by comparing the means over the first and second halves of each sampling interval; the resulting relative drift does not exceed 2 %.

3. Results and discussion

We first examine the global flow and heat-transport characteristics of the vibrated two-phase system. Figure 2(*a–c*) shows three-dimensional distributions of the dispersed phase at three representative Weber numbers and figure 2(*d–f*) shows the corresponding three-dimensional temperature fields. At low Weber number (figure 2*a*,*d*; $We = 0.1$), capillarity suppresses large interfacial deformation and the two fluids remain nearly stratified, so the temperature field retains a layered structure.

As We increases (figure 2*b*,*e*; $We = 2$), the capillary constraint is weakened and the interface develops pronounced bulging, accompanied by a stronger distortion of the thermal field near the interface. At much larger We (figure 2*c*,*f*; $We = 1000$), the dispersed phase is no longer anchored to the initial layer and forms a droplet-dispersed morphology, producing a different thermal organisation around the mobile dispersed structures. These snapshots therefore suggest three distinct morphological states: a stratified-layer state, an interfacial-bulging state and a droplet-dispersed state, consistent with the broader observation that interfacial structure can organise distinct transport states in thermally

https://doi.org/10.1017/jfm.2026.12243

driven multiphase flows (Liu *et al.* 2022*b*; Pelusi *et al.* 2025*b*). Representative time-dependent evolution within these states is shown in supplementary movies 1–3 available at https://doi.org/10.1017/jfm.2026.12243 at $We = 1$, 10 and 1000, respectively.

The change in flow structure can also be reflected in the transport response. In the present work, the reported Nusselt number is taken as $Nu = (Nu_{top} + Nu_{bot})/2$, where the wall values are defined from the conductivity-weighted heat flux as

$$Nu_{top,bot} = \frac{\langle -k\,\partial_z T\rangle_{top,bot}}{k_{eff}\Delta/H}. \tag{3.1}$$

Here, $\langle\cdot\rangle$ denotes averaging along the corresponding wall, $k_{eff} = H/(H_0/k_0 + H_1/k_1)$ is the effective conductivity of the initial two-layer conductive state, and H_0 and H_1 are the initial thicknesses of fluids 0 and 1, following the same series-conduction normalisation used for biphasic thermal convection (Wang *et al.* 2020*b*). Since $k_1/k_0 = 1$ in the present cases, $k_{eff} = k_0$; in dimensionless form, this reduces to $Nu_{top,bot} = \langle -\tilde{k}\partial_z\theta\rangle_{top,bot}$. The Reynolds number is defined as $Re = U_{rms}H/\nu_0$, with $U_{rms} = \langle \boldsymbol{u}\cdot\boldsymbol{u}\rangle_{V,t}^{1/2}$ (Zhang *et al.* 2017; Wu *et al.* 2022).

The corresponding transport data in figures 2(*g*) and 2(*h*) exhibit three distinct trends, each associated with one of the flow states identified earlier. In the stratified-layer state (figure 2*a*,*d*), the system remains essentially a two-layer flow and the temperature field retains a layered structure. Over this interval, the transport response remains associated with the stratified thermal structure, while *Re* changes only weakly. When interfacial bulging develops (figure 2*b*,*e*), hot fluid is lifted and cold fluid penetrates downward, opening an efficient cross-interface transport channel and producing the sharp rise of *Nu*. The lifted dispersed phase, however, intrudes into the bulk and obstructs the previously coherent circulation, converting part of the motion into interfacial deformation and confined recirculation; as a result, *Re* decreases. In the droplet-dispersed state (figure 2*c*,*f*), detached droplets move vertically through the cell and carry heat between the hot and cold regions, thereby enhancing vertical heat transport and keeping *Nu* high. At the same time, the coherent large-scale circulation is further broken into local recirculation, interfacial motion and droplet-scale motion, so that the volume-averaged *Re* remains low, consistent with previous observations that dispersed droplets or bubbles can modify vortical structures, velocity fluctuations and dissipation in multiphase thermal flows (Magnaudet & Eames 2000; Yuge & Hagiwara 2004; Lakkaraju *et al.* 2011; Qi *et al.* 2026). The representative three-dimensional results show a slightly higher *Nu* and an earlier decrease in *Re* than their two-dimensional counterparts (figure 2*g*,*h*). A similar dimensional trend has been reported in Rayleigh–Bénard convection, where planar confinement strengthens the large-scale circulation and increases *Re* without necessarily enhancing *Nu* (van der Poel *et al.* 2013). In the present system, spanwise freedom may weaken the coherent circulation while allowing spatially distributed interfacial and droplet motion to sustain vertical heat transport. Thus, *Nu* is controlled mainly by the availability of cross-interface heat pathways, whereas *Re* measures the coherence of the global flow. Although *Nu* and *Re* depend on the vibration frequency even at fixed Ra_{vib}, the sequence of interfacial states is retained over the tested range (Appendix C). To characterise the three states locally, we examine the wall-normal profiles of the temperature and vertical-velocity fluctuations,

$$T_{rms}(z) = \left\langle \left[T - \langle T\rangle_{x,t}\right]^2\right\rangle_{x,t}^{1/2}, \qquad w_{rms}(z) = \left\langle \left[w - \langle w\rangle_{x,t}\right]^2\right\rangle_{x,t}^{1/2}. \tag{3.2}$$

https://doi.org/10.1017/jfm.2026.12243

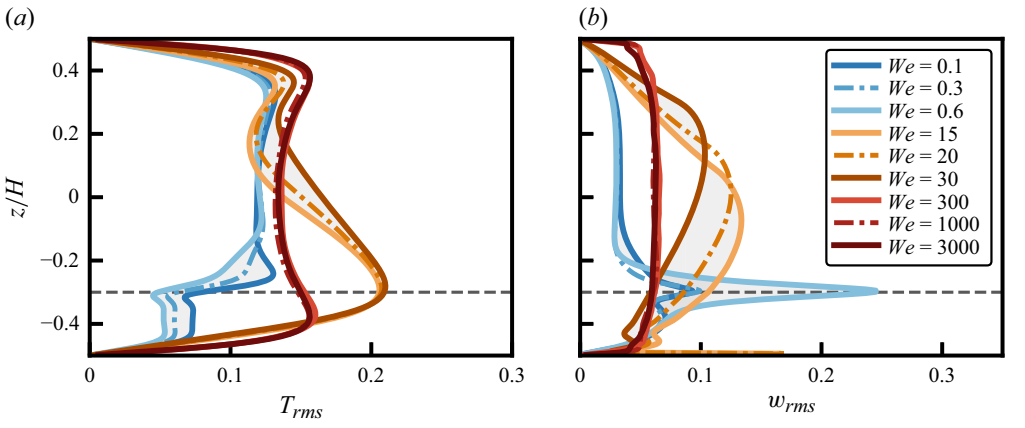


Figure 3. Wall-normal profiles of (*a*) T_{rms} and (*b*) w_{rms} for $\alpha_1/\alpha_0 = 4$. Blue, orange and red denote the stratified-layer ($We = 0.1$, 0.3 and 0.6), interfacial-bulging ($We = 15$, 20 and 30) and droplet-dispersed ($We = 300$, 1000 and 3000) states, respectively. Solid curves bound the shaded range in each state and the intermediate case is dash-dotted. The horizontal dashed line marks the initial interface position $z/H = -0.3$.

Here, $\langle\cdot\rangle_{x,t}$ denotes horizontal and temporal averaging over the statistically stationary interval. Figure 3 provides distinct local signatures of the three states. In the stratified state, w_{rms} is localised near the initial interface and T_{rms} varies markedly across it. Bulging extends both fluctuations into the bulk, whereas the droplet-dispersed state exhibits broader profiles that are nearly symmetric about the midplane. We next examine the transition thresholds separating these states.

To quantify these transitions, we define $\mathcal{D}_+ = \{\boldsymbol{x} \in \mathcal{D} : z > z_0\}$ as the portion of the computational domain above the reference height z_0. The elevated dispersed-phase fraction is then given by

$$M_{det}(t) = \frac{\displaystyle\int_{\mathcal{D}_+} C(\boldsymbol{x}, t)\, \mathrm{d}\boldsymbol{x}}{\displaystyle\int_{\mathcal{D}} C(\boldsymbol{x}, t)\, \mathrm{d}\boldsymbol{x}}. \tag{3.3}$$

Here, $\mathrm{d}\boldsymbol{x}$ denotes an area element in two dimensions and a volume element in three dimensions. In the present geometry, z_0 coincides with the initial interface position, namely $z_0 = -0.3$. The reported value is obtained by evaluating $M_{det}(t)$ from instantaneous fields and averaging over the statistically stationary interval. We use this quantity to characterise the degree of bulging of the dispersed phase above the reference height. By definition, $M_{det} = 0$ corresponds to an ideal layered state in which the dispersed phase remains below the reference height z_0. At the other extreme, once the detached droplet is no longer trapped near the lower layer, it travels back and forth between the two plates under the vibration-driven flow; as a result, its time-averaged vertical distribution becomes approximately uniform, and one then expects $M_{det} \approx 0.8$ because the subdomain $z > z_0$ occupies 80 % of the cell height in the present geometry.

The measured M_{det} is shown in figure 4(*b*) as a function of We for different α_1/α_0. For each thermal-expansion ratio α_1/α_0, M_{det} remains small in the stratified-layer regime and increases once interfacial bulging develops. Here, $We_{c,bulging}$ is identified from figure 4(*b*) using the small threshold $M_{det} = 0.03$, which separates the nearly stratified branch from the bulging branch. The same elevated dispersed-phase fraction is also used to define the droplet-detachment threshold, $We_{c,det}$, using $M_{det} = 0.79$, which marks the transition

https://doi.org/10.1017/jfm.2026.12243

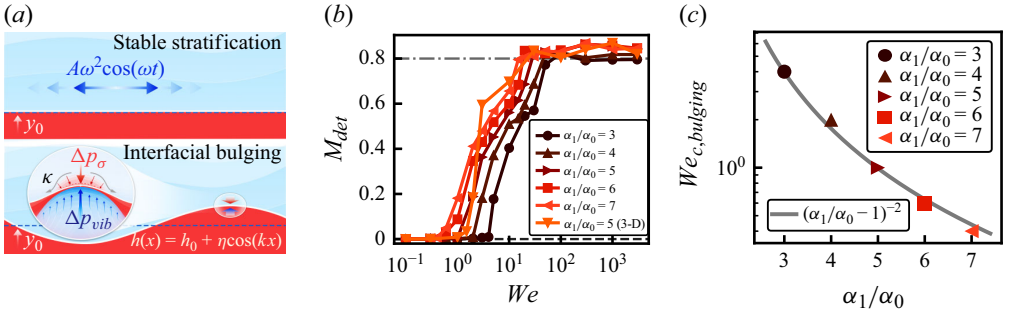


Figure 4. (*a*) Schematic of the onset of interfacial bulging in the vibrated two-phase layer. A weakly perturbed interface, $z_s(x) = z_0 + \eta\cos(k_m x)$, becomes unstable when the thermovibrational pressure difference Δp_{vib} overcomes the capillary restoring stress represented by Δp_σ. (*b*) Elevated dispersed-phase fraction M_{det} as a function of We for different thermal-expansion contrasts α_1/α_0, from which the critical Weber number $We_{c,bulging}$ for interfacial bulging is determined. Representative three-dimensional data at $\alpha_1/\alpha_0 = 5$ are included for comparison. Here, M_{det} denotes the fraction of the dispersed phase located above the reference height z_0. (*c*) Critical Weber number $We_{c,bulging}$ plotted against α_1/α_0. The decrease of $We_{c,bulging}$ with increasing α_1/α_0 is compared with the scaling prediction $We_{c,bulging} \sim (\alpha_1/\alpha_0 - 1)^{-2}$ (grey curve).

to the droplet-dispersed branch. This second threshold will be discussed later. We first focus on the onset of interfacial bulging. Figure 4(*c*) shows that $We_{c,bulging}$ decreases monotonically as α_1/α_0 increases, indicating that a larger thermal-expansion contrast destabilises the interface at a smaller Weber number.

To explain this trend, we estimate the onset condition from a balance between the thermovibrational pressure difference and capillary restoring stress at the interface (figure 4*a*). When the two fluids have different thermal-expansion coefficients, the imposed vibration produces unequal thermovibrational responses on the two sides of the interface. The dimensional relative velocity can be estimated as $U^*_{int} \sim (\alpha_1 - \alpha_0)A\Omega\Delta T$, or equivalently, $U^*_{int} \sim (\alpha_1/\alpha_0 - 1)U_v$ with $U_v = \alpha_0 A\Omega\Delta T$.

For a weakly perturbed interface $z^*_s(x^*) = z^*_0 + \eta^*\cos(k^*_m x^*)$, the thermovibrational pressure difference has the dimensional scale

$$\Delta p^*_{vib} \sim \rho_0 U^{*2}_{int}\frac{\eta^*}{H} \sim \rho_0 U_v^2\left(\frac{\alpha_1}{\alpha_0} - 1\right)^2\frac{\eta^*}{H}. \tag{3.4}$$

The capillary restoring pressure is set by the curvature perturbation. Since $\kappa^* \sim k^{*2}_m\eta^*$ for this mode, its dimensional scale is

$$\Delta p^*_\sigma \sim \sigma k^{*2}_m\eta^*. \tag{3.5}$$

At the onset of interfacial bulging, these two dimensional pressure scales balance,

$$\rho_0 U_v^2\left(\frac{\alpha_1}{\alpha_0} - 1\right)^2\frac{\eta^*}{H} \sim \sigma k^{*2}_m\eta^*. \tag{3.6}$$

Introducing $We = \rho_0 U_v^2 H/\sigma$ and $k_m = k^*_m H$, this balance gives

$$We_{c,bulging}\left(\frac{\alpha_1}{\alpha_0} - 1\right)^2 \sim k_m^2, \qquad We_{c,bulging} \sim k_m^2\left(\frac{\alpha_1}{\alpha_0} - 1\right)^{-2}. \tag{3.7}$$

For the present fixed geometry and initial layer height, the lowest mode, corresponding to the dimensionless wavenumber $k_m = k^*_m H \simeq 1$, is expected to become unstable first, because it requires the smallest capillary restoring pressure in the above-mentioned

https://doi.org/10.1017/jfm.2026.12243

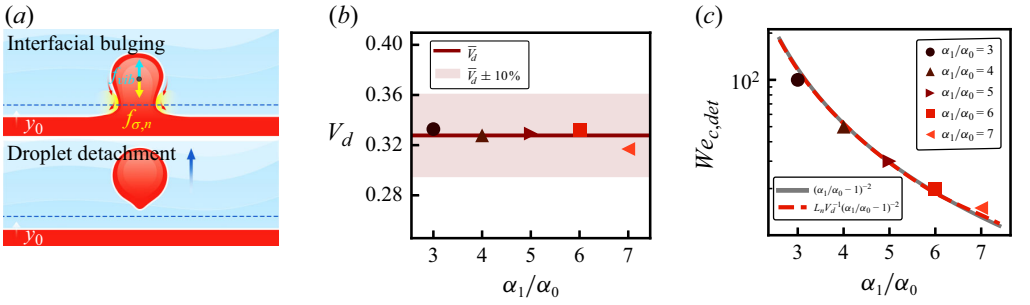


Figure 5. (*a*) Schematic of the second transition from interfacial bulging to droplet detachment. The lifted liquid volume V_d is driven by the effective thermovibrational force, while the capillary force retaining the remaining neck is characterised by a contact length L_n. (*b*) Measured V_d at the droplet-detachment threshold $We_{c,det}$ as a function of the thermal-expansion contrast α_1/α_0. The shaded band denotes the mean value with a $\pm 10\,\%$ variation, showing that V_d varies only weakly over the range considered. (*c*) Droplet-detachment threshold $We_{c,det}$ as a function of α_1/α_0. The grey curve shows the leading-order scaling $C_f(\alpha_1/\alpha_0 - 1)^{-2}$ with fitted prefactor C_f, while the dashed curve includes the geometric correction $L_n V_d^{-1}(\alpha_1/\alpha_0 - 1)^{-2}$, with V_d measured at the detachment threshold and L_n treated as approximately constant.

balance. This is also the onset mode observed in the simulations. The corresponding wavenumber factor can therefore be absorbed into the prefactor, giving

$$We_{c,bulging} \sim \left(\frac{\alpha_1}{\alpha_0} - 1\right)^{-2}. \tag{3.8}$$

This reduced form provides a direct comparison with the critical Weber numbers extracted from the elevated dispersed-phase fraction. As shown in figure 4(*c*), the measured thresholds follow the predicted decrease with increasing α_1/α_0, indicating that the onset of interfacial bulging is well described by the pressure–capillary balance. It should be noted that this scaling estimate retains only the interfacial pressure imbalance caused by the thermal-expansion mismatch, while neglecting temperature-induced density variations within each layer, which may also contribute to the thermovibrational pressure variation.

We next consider the second transition point, at which the lifted dispersed-phase structure loses its neck connection to the lower layer. This transition corresponds to the change from the interfacial-bulging state to droplet detachment. At this stage, the interface is no longer a small-amplitude perturbation, but has formed a finite-amplitude elevated liquid structure that remains connected to the lower layer through a thin neck. Droplet detachment occurs when this neck connection is broken (figure 5*a*). The corresponding time-dependent evolution at $We = 200$ is shown in supplementary movie 4. Such loss of interfacial connectivity is known to reorganise multiphase dynamics (Soligo *et al.* 2019; Liu *et al.* 2021*a*). The controlling balance is therefore different from that for the first transition: interfacial bulging is governed by a pressure–capillary balance for a weak deformation, whereas droplet detachment is governed by a force balance between the thermovibrational force acting on the lifted liquid volume and the capillary force retaining the remaining neck.

The thermovibrational force responsible for detachment can be written schematically as the sum of two contributions, $F^*_{vib} \sim F^*_{base} + F^*_{contrast}$. The baseline term represents the phase-common thermovibrational response and has the reference inertial-force scale $F^*_{base} \sim (\rho_0 U_v^2/H)V_d^*$. The second term arises from the mismatch of the thermovibrational response across the interface. This mismatch produces an oscillatory body-force

https://doi.org/10.1017/jfm.2026.12243

difference of order $\Delta f^*_{vib,inst} \sim \rho_0(\alpha_1 - \alpha_0)A\Omega^2\Delta T$ and a relative vibration velocity $U^*_{rel} \sim (\alpha_1 - \alpha_0)A\Omega\Delta T$. Since the instantaneous contribution changes sign over a vibration period, the leading averaged inertial contribution is quadratic in U^*_{rel}, giving $F^*_{contrast} \sim (\rho_0 U_v^2/H)(\alpha_1/\alpha_0 - 1)^2 V_d^*$. Thus, the contrast-dependent term sets the leading dependence of the detachment threshold on α_1/α_0, while the baseline and lower-order terms are absorbed into the prefactor. The detailed derivation of these force scales is given in Appendix D.

The reduced detachment balance therefore involves the following dimensional force scales:

$$F^*_{contrast} \sim \frac{\rho_0 U_v^2}{H}\left(\frac{\alpha_1}{\alpha_0} - 1\right)^2 V_d^*, \qquad F^*_\sigma \sim \sigma L_n^*, \tag{3.9}$$

where V_d^* is the dimensional lifted volume and L_n^* is the dimensional contact length of the neck. Balancing these forces, and using $We = \rho_0 U_v^2 H/\sigma$, $L_n = L_n^*/H$ and $V_d = V_d^*/H^3$ gives

$$We_{c,det} \sim \frac{L_n}{V_d}\left(\frac{\alpha_1}{\alpha_0} - 1\right)^{-2}. \tag{3.10}$$

Here, the ratio L_n/V_d is retained as the geometric factor controlling the capillary retention of the neck. In the two-dimensional calculations, the force balance is interpreted per unit span, so the capillary factor associated with the neck is an order-one constant and the measured V_d is the lifted area, equivalently, the lifted volume per unit span. In three dimensions, L_n denotes the contact-line length of the neck and V_d the lifted volume. The three-dimensional calculation in figure 2(*c*) indicates weak spanwise development during detachment; for the present spanwise extent, this gives an approximately constant L_n of order unity, approximately 2 if the two sides of the neck are counted. Thus, the difference between the two- and three-dimensional measures mainly affects the prefactor. As shown in figure 5(*b*), V_d at the detachment threshold changes only weakly with α_1/α_0. Thus, the leading dependence reduces to $We_{c,det} \sim (\alpha_1/\alpha_0 - 1)^{-2}$. Figure 5(*c*) confirms this trend: the reduced scaling captures the systematic decrease of $We_{c,det}$, while including the measured V_d^{-1} correction gives an almost overlapping curve. The second transition is therefore controlled mainly by the same contrast-dependent forcing as the first transition, with a different prefactor set by finite-amplitude detachment and neck retention. More generally, the offset between the two thresholds scales as $L_n/(V_d k_m^2)$ and need not remain constant when the domain geometry is varied, because changes in the domain width, height or spanwise extent may alter the onset mode k_m, the lifted volume or the neck geometry.

To assess how these two thresholds organise the global transport response, we replot the data against the corresponding normalised Weber numbers. Figure 6(*a*,*b*) shows *Nu* and *Re* as functions of $We/We_{c,bulging}$. Under this normalisation, the first transition is aligned near $We/We_{c,bulging} = 1$, so that the onset of interfacial bulging can be compared directly across different thermal-expansion contrasts. The Nusselt number begins to rise rapidly once this threshold is crossed, whereas the Reynolds number continues to evolve over a broader range. This indicates that $We_{c,bulging}$ captures the onset of strong interfacial deformation, but not the later transition to droplet detachment.

Figure 6(*c*,*d*) instead shows the same data as functions of $We/We_{c,det}$. Under this normalisation, the second transition is aligned near $We/We_{c,det} = 1$. The Nusselt number remains elevated across this transition, whereas the Reynolds number drops sharply and then approaches a lower level after droplet detachment. This decrease of *Re* indicates that,

https://doi.org/10.1017/jfm.2026.12243

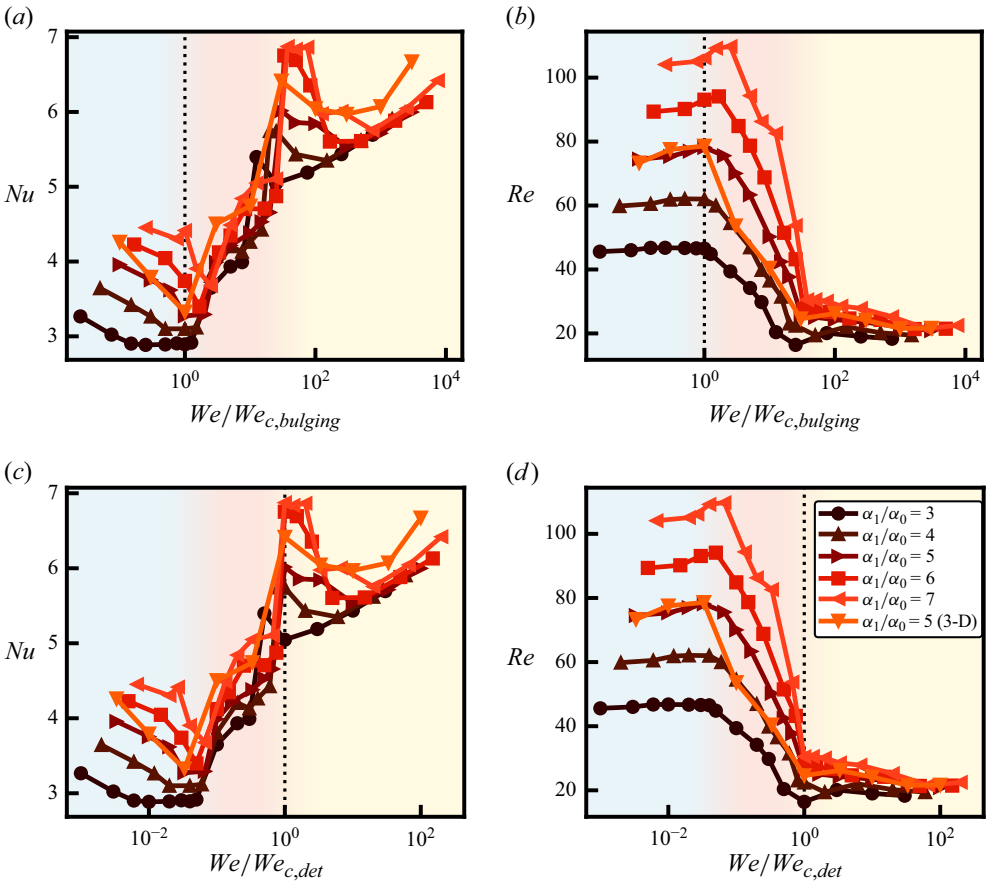


Figure 6. (*a*) Nusselt number *Nu* and (*b*) Reynolds number *Re* as functions of $We/We_{c,bulging}$ for different thermal-expansion contrasts α_1/α_0. (*c*) Nusselt number *Nu* and (*d*) Reynolds number *Re* as functions of $We/We_{c,det}$. The coloured background indicates the three regimes: stratified-layer, interfacial-bulging and droplet-dispersed states. The dotted vertical line marks the corresponding normalised threshold, namely $We/We_{c,bulging} = 1$ in panels (*a*) and (*b*), and $We/We_{c,det} = 1$ in panels (*c*) and (*d*).

once the neck connection is lost, the dispersed phase no longer supports the previous large-scale circulation, but instead behaves as mobile droplets that promote local recirculation and dissipation. Similar links between dispersed-phase structural reorganisation and the modulation of carrier-phase agitation have also been noted in other multiphase systems (Almeras *et al.* 2017; Yi *et al.* 2024). Taken together, figure 6 shows that the transport response is organised by two distinct thresholds: $We_{c,bulging}$ marks the onset of interfacial bulging, whereas $We_{c,det}$ marks droplet detachment through the loss of neck connectivity and the associated reorganisation of the global flow intensity.

The phase diagram corresponding to these two thresholds is summarised in figure 7(*a*). The symbols represent the simulated cases in the $(\alpha_1/\alpha_0, We)$ plane and the coloured regions distinguish the three regimes identified from the elevated dispersed-phase fraction M_{det}, namely the stratified-layer, interfacial-bulging and droplet-dispersed states. The lower boundary separates the stratified-layer and interfacial-bulging states, whereas the upper boundary marks the onset of droplet detachment. In this way, the phase diagram provides a compact summary of how the interfacial morphology evolves across the parameter space. Both boundaries shift to lower *We* as α_1/α_0 increases, confirming

https://doi.org/10.1017/jfm.2026.12243

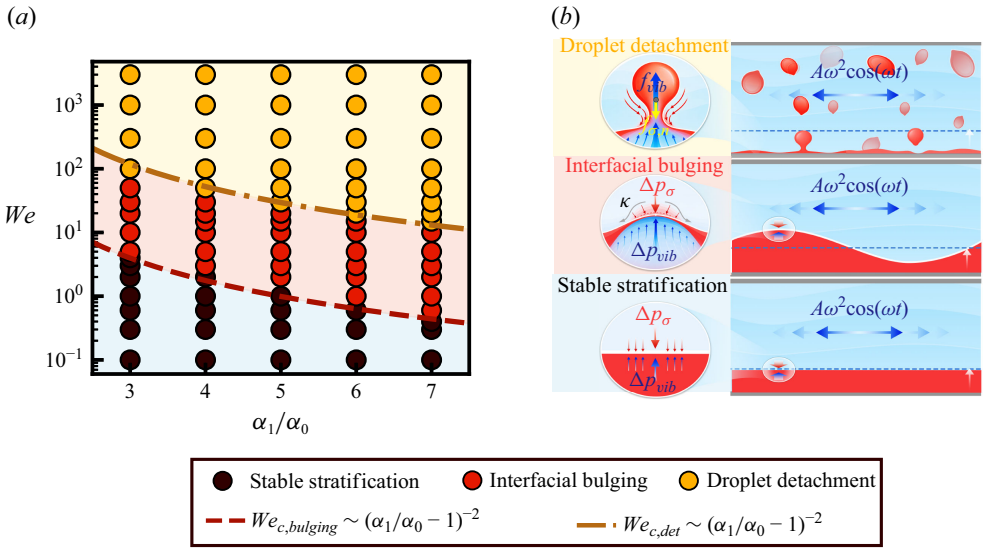


Figure 7. Regime map and physical summary of the vibration-driven interfacial transitions. (*a*) Regime map in the $(\alpha_1/\alpha_0, We)$ plane. The symbols denote the three regimes identified from the elevated dispersed-phase fraction M_{det}, and the dashed curves show the scaling boundaries $We_{c,bulging} \sim (\alpha_1/\alpha_0 - 1)^{-2}$ and $We_{c,det} \sim (\alpha_1/\alpha_0 - 1)^{-2}$. (*b*) Schematic summary of the corresponding flow states and local mechanisms. In the stratified-layer regime, capillary pressure suppresses interfacial deformation; in the interfacial-bulging regime, the thermovibrational pressure difference overcomes capillary restoring stress and produces a finite-amplitude interfacial deformation; in the droplet-dispersed regime, the neck connection is lost and detached droplets promote local recirculation in the bulk flow.

that a larger thermal-expansion contrast strengthens the thermovibrational interfacial forcing. The dashed curves show that the two boundaries are both well described by the same leading-order dependence on α_1/α_0, while remaining separated by a finite gap. This gap reflects the additional capillary force that has to be overcome before the remaining neck is lost. The accompanying schematics in figure 7(*b*) summarise the physical picture underlying the three regions: capillarity maintains a nearly flat interface in the stratified-layer regime, the thermovibrational pressure difference drives finite-amplitude deformation in the interfacial-bulging regime and the loss of neck connectivity in the droplet-dispersed regime turns the dispersed phase into mobile droplets that generate local recirculation. Figure 7 therefore connects the regime classification directly to the two scaling arguments and to the corresponding reorganisation of transport.

4. Conclusion

The central result is that interfacial connectivity reorganises vibration-induced heat and momentum transport, so that they do not vary in parallel. A nearly flat interface confines circulation within the individual layers and limits cross-interface heat exchange. Finite-amplitude bulging opens an effective vertical heat-transport pathway while disrupting the coherent circulation, causing *Nu* to increase as *Re* decreases. After detachment, mobile droplets continue to carry heat between the hot and cold regions even though the flow fragments into localised structures. Global flow intensity alone is therefore insufficient to characterise heat transport in this two-phase system.

The two transition conditions distinguish the small-amplitude onset of interfacial bulging from the finite-amplitude loss of phase connectivity. Bulging begins when

https://doi.org/10.1017/jfm.2026.12243

k_1/k_0	q_{ana}	q_{num}	Relative error (%)	k_1/k_0	q_{ana}	q_{num}	Relative error (%)
0.5	0.66667	0.66854	0.28	2	1.33333	1.32987	0.26
1	1.00000	1.00000	0.00	5	1.66667	1.65803	0.52

Table 1. Validation of stationary heat conduction through two immiscible liquid layers.

the thermovibrational pressure difference overcomes capillary restoring stress, whereas detachment additionally requires the thermovibrational force acting on the lifted liquid volume to overcome capillary retention at the remaining neck. The common contrast-dependent forcing shifts both thresholds in the same direction, while their finite separation reflects the distinct geometric factors governing deformation and neck rupture. These balances link material contrast and capillarity to the selected interfacial state and its transport response.

Representative three-dimensional calculations recover the same ordering of interfacial states and associated transport trends over the parameters examined, while the quantitative values of Nu and Re, and the transition locations depend on the spanwise geometry. The framework should therefore be interpreted within the tested parameter range and for temperature-independent surface tension. The main regime map and threshold scalings are based on $a = 0.01$; extending the frequency–amplitude comparison beyond the tested range, and determining how mode selection, spanwise extent and finite Marangoni stresses shift the regime boundaries remain important directions for future work.

Supplementary material and movies. Supplementary material and movies are available at https://doi.org/10.1017/jfm.2026.12243.

Funding. This work is supported by NSFC Excellence Research Group Program for 'Multiscale Problems in Nonlinear Mechanics' (No.12588201), and it was also supported by the Natural Science Foundation of China under grant nos. 12372219, 52450304, 12432011, 12422208, 12421002, 12372220 and 12502255, the China Postdoctoral Science Foundation under Grant No. 2024M761631, and the New Cornerstone Science Foundation through the New Cornerstone Investigator Program and the XPLORER PRIZE.

Declaration of interests. The authors report no conflict of interest.

Appendix A. Additional numerical verification

We validate the three numerical ingredients most relevant here: thermovibrational forcing, interfacial heat conduction and interface capture during breakup. Their coupled performance for an intact deformable interface is assessed separately in figure 1.

To isolate the thermovibrational forcing, we remove the interface and reproduce the single-phase microgravity calculations of Guo *et al.* (2023) at $Ra = 10^8$, $Pr = 4.38$ and $a = 0.01$, varying $10^3 \leqslant \omega \leqslant 3 \times 10^5$. Figure 8(*a*) reproduces the conductive limit, $Nu \approx 1$, and the overall enhancement of heat transport, supporting the implementation of the forcing and its coupling to the momentum and energy equations.

To test interfacial heat conduction, we suppress vibration and fluid motion, and consider two equal-depth immiscible layers, $H_0 = H_1 = H/2$. All property ratios are unity except $\lambda_k = k_1/k_0$, for which we use $\lambda_k = 0.5$, 1, 2 and 5. For $\Delta T = T_b - T_t$, the analytical series-conduction flux and the numerical wall flux are $q_{ana} = \Delta T/(H_0/k_0 + H_1/k_1)$ and $q_{num} = \langle (q_{bottom} + q_{top})/2 \rangle_t$, respectively. Their relative difference remains below 0.52 % (table 1), confirming the conductive energy balance across the interface.

To assess interface capture during breakup, we reproduce the benchmark of Liu *et al.* (2021*a*) at $Ra = 10^8$, $Pr = 1$ and $We = 1.6 \times 10^4$, with unit material-property ratios. The

https://doi.org/10.1017/jfm.2026.12243

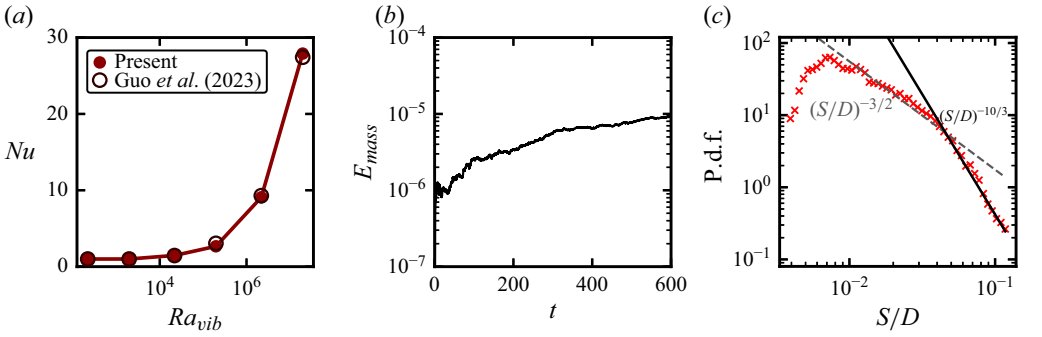
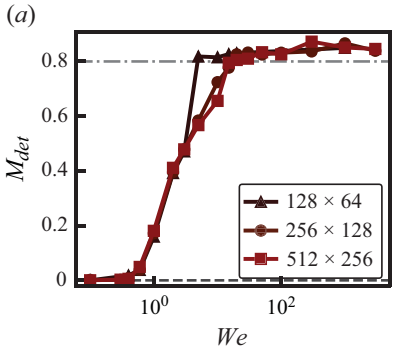


Figure 8. (*a*) Nusselt number as a function of Ra_{vib} for single-phase thermovibrational convection under microgravity, compared with the numerical data of Guo *et al.* (2023). (*b*) Relative dispersed-phase volume error, $E_{mass} = |V_{disp}(t) - V_{disp}(0)|/V_{disp}(0)$. (*c*) Probability density function of the normalised droplet size S/D; the dashed and solid lines denote the $(S/D)^{-3/2}$ and $(S/D)^{-10/3}$ reference slopes, respectively.



(*b*)

Case	Grid resolution	*Nu*	*Re*
G1	128 × 64	6.49	25.11
G2	256 × 128	6.16	23.62
G3	512 × 256	6.05	21.56
G4	1024 × 512	5.95	21.39

Figure 9. Grid-refinement tests at $\alpha_1/\alpha_0 = 7$. (*a*) Elevated dispersed-phase fraction M_{det} as a function of *We* on three grids; the horizontal reference levels $M_{det} = 0$ and 0.8 denote the ideal layered limit and the approximately uniform vertical distribution expected after detachment, respectively. (*b*) Time-averaged *Nu* and *Re* at $We = 1000$ on four grids.

dispersed-phase volume error remains below 9.4×10^{-6} (figure 8*b*). The droplet-size distribution is consistent with the $(S/D)^{-3/2}$ capillary-breakup range (Deane & Stokes 2002) and the $(S/D)^{-10/3}$ turbulence-fragmentation range (Garrett *et al.* 2000; Yu *et al.* 2020; Liu *et al.* 2021*a*) (figure 8*c*), with a cross-over associated with the Hinze scale (Hinze 1955). These results support dispersed-phase conservation and the representation of breakup over the resolved size range.

Appendix B. Grid-convergence assessment

We assess grid dependence at $\alpha_1/\alpha_0 = 7$ using both the transition curve and the global transport statistics. Figure 9(*a*) shows that the 128×64 grid predicts earlier detachment, whereas the 256×128 and 512×256 curves are closely aligned; their sampled detachment thresholds differ by one *We* interval. At $We = 1000$, the *Nu* and *Re* values on the 512×256 production grid are also close to those on the finest 1024×512 grid (figure 9*b*). The agreement in the state sequence, transition range and global transport statistics supports the production-grid resolution used here.

https://doi.org/10.1017/jfm.2026.12243

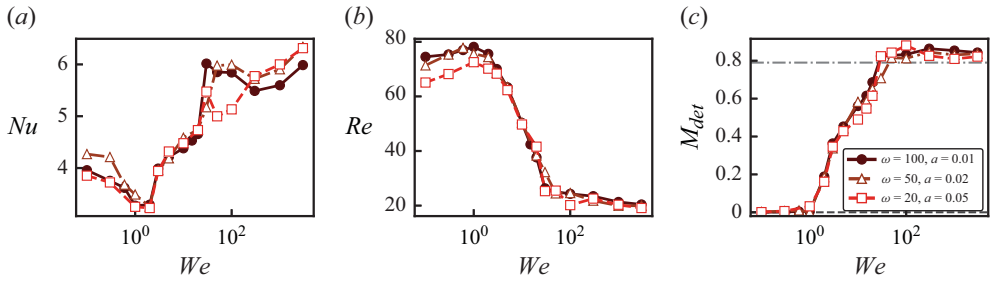


Figure 10. Influence of vibration frequency at fixed $Ra_{vib} = 10^5$ and $\alpha_1/\alpha_0 = 5$. (*a*) Nusselt number Nu, (*b*) Reynolds number Re and (*c*) elevated dispersed-phase fraction M_{det} as functions of We for $\omega = 100$, 50 and 20, corresponding to $a = 0.01$, 0.02 and 0.05, respectively.

Appendix C. Influence of the vibration frequency

To assess the influence of vibration frequency at fixed forcing intensity, we compare Weber-number sweeps at $Ra_{vib} = 10^5$ and $\alpha_1/\alpha_0 = 5$ for $\omega = 100$, 50 and 20. The corresponding amplitudes are $a = 0.01$, 0.02 and 0.05, respectively, since $\omega = a^{-1}$ under the present scaling. The amplitude is therefore adjusted as the frequency is varied to maintain the same vibrational Rayleigh number.

Figure 10 shows quantitative differences in Nu and Re, particularly at low We and near droplet detachment, indicating that Ra_{vib} alone does not determine the transport response. Nevertheless, the M_{det} curves retain the progression from stratification through interfacial bulging to droplet dispersion, with transitions occurring over comparable Weber-number ranges. These results support the persistence of the state sequence over the tested frequencies, but the finite We sampling does not establish frequency-independent critical thresholds.

Appendix D. Scaling estimate for the thermovibrational detachment force

This appendix summarises the scaling argument used to estimate the effective thermovibrational force responsible for droplet detachment. We first write the relevant estimates in dimensional form and then introduce the non-dimensional Weber number through the final force balance. The imposed horizontal vibration has a displacement scale A and angular frequency Ω, so that the acceleration scale is $A\Omega^2$. In a thermally stratified fluid, the oscillatory inertial body-force density associated with thermal expansion has the scale

$$f^*_{vib,inst} \sim \rho_0 \alpha A \Omega^2 \Delta T. \tag{D1}$$

For the two-phase system, the common part of this response gives a baseline thermovibrational driving. The additional driving relevant to interfacial deformation and detachment comes from the mismatch across the interface. Its instantaneous dimensional scale is

$$\Delta f^*_{vib,inst} \sim \rho_0 (\alpha_1 - \alpha_0) A \Omega^2 \Delta T. \tag{D2}$$

This contribution changes sign over a vibration period. The associated relative vibration velocity accumulated over one oscillation period is estimated as

$$U^*_{rel} \sim \frac{\Delta f^*_{vib,inst}}{\rho_0 \Omega} \sim (\alpha_1 - \alpha_0) A \Omega \Delta T. \tag{D3}$$

https://doi.org/10.1017/jfm.2026.12243

With the vibration velocity scale $U_v = \alpha_0 A\Omega\Delta T$, the same estimate can be written as

$$U^*_{rel} \sim U_v \left(\frac{\alpha_1}{\alpha_0} - 1\right). \tag{D4}$$

The first-order oscillatory velocity has zero mean over a vibration period. The leading non-zero averaged inertial contribution is therefore quadratic in the relative velocity. Using H as the characteristic length of the lifted structure, the corresponding inertial acceleration scale is

$$a^*_{in} \sim \frac{U^{*2}_{rel}}{H} \sim \frac{U^2_v}{H}\left(\frac{\alpha_1}{\alpha_0} - 1\right)^2. \tag{D5}$$

This inertial response gives an effective contrast-dependent force density of order $\rho_0 a^*_{in}$. For a dimensional lifted volume V^*_d, the corresponding driving force has the scale

$$F^*_{contrast} \sim \frac{\rho_0 U^2_v}{H}\left(\frac{\alpha_1}{\alpha_0} - 1\right)^2 V^*_d, \tag{D6}$$

where the order-one coefficient associated with this projection is introduced below in the complete force balance. The common thermovibrational response gives a baseline contribution with the same reference inertial-force scale,

$$F^*_{base} \sim \frac{\rho_0 U^2_v}{H} V^*_d, \tag{D7}$$

where the order-one coefficient associated with this baseline response is introduced below in the complete force balance. The complete dimensional driving force may therefore be written as

$$F^*_{vib} \sim \frac{\rho_0 U^2_v}{H}\left[B + C\left(\frac{\alpha_1}{\alpha_0} - 1\right)^2\right] V^*_d. \tag{D8}$$

The first term is the baseline thermovibrational contribution, while the second term is the contrast-dependent inertial contribution. This complete form gives a finite threshold in the low-contrast limit through B.

The variation of the detachment threshold with thermal-expansion contrast is governed by the contrast-dependent inertial contribution. Let $r = \alpha_1/\alpha_0$. This contribution is of order $O[(r-1)^2]$, whereas the baseline and lower-order contributions mainly provide weak offsets or prefactor corrections. In this contrast-dominated limit, the reduced dimensional driving force is

$$F^*_{vib} \sim \frac{\rho_0 U^2_v}{H}\left(\frac{\alpha_1}{\alpha_0} - 1\right)^2 V^*_d. \tag{D9}$$

The resisting force is the capillary force retaining the remaining neck,

$$F^*_\sigma \sim \sigma L^*_n, \tag{D10}$$

where L^*_n is the dimensional contact length of the neck. Balancing the dimensional driving and resisting forces gives

$$\frac{\rho_0 U^2_v}{H}\left(\frac{\alpha_1}{\alpha_0} - 1\right)^2 V^*_d \sim \sigma L^*_n. \tag{D11}$$

https://doi.org/10.1017/jfm.2026.12243

We now introduce the non-dimensional quantities $We = \rho_0 U_v^2 H/\sigma$, $L_n = L_n^*/H$ and $V_d = V_d^*/H^3$. The force balance then becomes

$$We\left(\frac{\alpha_1}{\alpha_0} - 1\right)^2 V_d \sim L_n, \tag{D12}$$

and the corresponding droplet-detachment threshold is

$$We_{c,det} \sim \frac{L_n}{V_d}\left(\frac{\alpha_1}{\alpha_0} - 1\right)^{-2}, \tag{D13}$$

up to a prefactor. The comparison in figure 5(*c*) shows that the measured droplet-detachment thresholds are well captured by this reduced form, further supporting the simplification over the parameter range considered.

References

Ahlers, G., Grossmann, S. & Lohse, D. 2009 Heat transfer and large scale dynamics in turbulent Rayleigh–Bénard convection. *Rev. Mod. Phys.* **81** (2), 503–537.

Almeras, E., Mathai, V., Lohse, D. & Sun, C. 2017 Experimental investigation of the turbulence induced by a bubble swarm rising within incident turbulence. *J. Fluid Mech.* **825**, 1091–1112.

Bakhuis, D., Ezeta, R., Bullee, P.A., Marin, A., Lohse, D., Sun, C. & Huisman, S.G. 2021 Catastrophic phase inversion in high-Reynolds-number turbulent Taylor–Couette flow. *Phys. Rev. Lett.* **126** (6), 064501.

Beysens, D. 2006 Vibrations in space as an artificial gravity? *Europhys. News* **37** (3), 22–25.

Beysens, D., Chatain, D., Evesque, P. & Garrabos, Y. 2005 High-frequency driven capillary flows speed up the gas–liquid phase transition in zero-gravity conditions. *Phys. Rev. Lett.* **95**, 034502.

Chillà, F. & Schumacher, J. 2012 New perspectives in turbulent Rayleigh–Bénard convection. *Eur. Phys. J. E* **35** (7), 58.

Cisse, I., Bardan, G. & Mojtabi, A. 2004 Rayleigh–Bénard convective instability of a fluid under high-frequency vibration. *Intl J. Heat Mass Transfer* **47** (19–20), 4101–4112.

Deane, G.B. & Stokes, M.D. 2002 Scale dependence of bubble creation mechanisms in breaking waves. *Nature* **418**, 839–844.

Demou, A.D., Scapin, N., Crialesi-Esposito, M., Costa, P., Spiga, F. & Brandt, L. 2024 Effects of Rayleigh and Weber numbers on two-layer turbulent Rayleigh–Bénard convection. *J. Fluid Mech.* **996**, A23.

Fan, Y., Zhang, Y.B., Su, J., Yi, L., Wang, C. & Sun, C. 2025 Experimental study of velocity statistics in wall-bounded turbulent emulsions. *J. Fluid Mech.* **1011**, A14.

Garrett, C., Li, M. & Farmer, D. 2000 The connection between bubble size spectra and energy dissipation rates in the upper ocean. *J. Phys. Oceanogr.* **30**, 2163–2171.

Gershuni, G.Z. & Lyubimov, D.V. 1998 *Thermal Vibrational Convection*. John Wiley & Sons.

Gershuni, G.Z., Zhukhovitskii, E.M. & Yurkov, Y.S. 1982 Vibrational thermal convection in a rectangular cavity. *Fluid Dyn.* **17** (4), 565–569.

Guan, J.H., Tamim, S.I., Magoon, C.W., Stone, H.A. & Sáenz, P.J. 2025 Galloping bubbles. *Nat. Commun.* **16**, 1572.

Guo, X.L., Wu, J.Z., Wang, B.F., Zhou, Q. & Chong, K.L. 2023 Flow structure transition in thermal vibrational convection. *J. Fluid Mech.* **974**, A29.

Hinze, J.O. 1955 Fundamentals of the hydrodynamic mechanism of splitting in dispersion processes. *AIChE J.* **1**, 289–295.

Hirata, K., Sasaki, T. & Tanigawa, H. 2001 Vibrational effects on convection in a square cavity at zero gravity. *J. Fluid Mech.* **445**, 327–344.

Hori, N., Ng, C.S., Lohse, D. & Verzicco, R. 2023 Interfacial-dominated torque response in liquid–liquid Taylor–Couette flows. *J. Fluid Mech.* **956**, A15.

Huang, Z.L., Guo, X.L., Wu, J.Z., Wang, B.F., Chong, K.L. & Zhou, Q. 2023 Rayleigh-number dependence of the critical vibration frequency in vibrating thermal turbulence. *Phys. Rev. Fluids* **8**, 113501.

Huang, Z.L., Wu, J.Z., Guo, X.L., Zhao, C.B., Wang, B.F., Chong, K.L. & Zhou, Q. 2024 Unifying constitutive law of vibroconvective turbulence in microgravity. *J. Fluid Mech.* **987**, A14.

https://doi.org/10.1017/jfm.2026.12243

LAKKARAJU, R., SCHMIDT, L.E., ORESTA, P., TOSCHI, F., VERZICCO, R., LOHSE, D. & PROSPERETTI, A. 2011 Effect of vapor bubbles on velocity fluctuations and dissipation rates in bubbly Rayleigh–Bénard convection. *Phys. Rev. E* **84** (3), 036312.

LAPPA, M. 2009 *Thermal Convection: Patterns, Evolution and Stability*. John Wiley & Sons.

LIU, H.R., CHONG, K.L., NG, C.S., VERZICCO, R. & LOHSE, D. 2022*a* Enhancing heat transport in multiphase Rayleigh–Bénard turbulence by changing the plate–liquid contact angles. *J. Fluid Mech.* **933**, R1.

LIU, H.R., CHONG, K.L., WANG, Q., NG, C.S., VERZICCO, R. & LOHSE, D. 2021*a* Two-layer thermally driven turbulence: mechanisms for interface breakup. *J. Fluid Mech.* **913**, A9.

LIU, H.R., CHONG, K.L., YANG, R., VERZICCO, R. & LOHSE, D. 2022*b* Heat transfer in turbulent Rayleigh–Bénard convection through two immiscible fluid layers. *J. Fluid Mech.* **938**, A31.

LIU, H.R., CHONG, K.L., YANG, R., VERZICCO, R. & LOHSE, D. 2022*c* Turbulent Rayleigh–Bénard convection with bubbles attached to the plate. *J. Fluid Mech.* **945**, A29.

LIU, H.R., NG, C.S., CHONG, K.L., LOHSE, D. & VERZICCO, R. 2021*b* An efficient phase-field method for turbulent multiphase flows. *J. Comput. Phys.* **446**, 110659.

LOHSE, D. 2022 Fundamental fluid dynamics challenges in inkjet printing. *Annu. Rev. Fluid Mech.* **54** (1), 349–382.

LOHSE, D. & SHISHKINA, O. 2023 Ultimate turbulent thermal convection. *Phys. Today* **76** (11), 26–32.

LOHSE, D. & SHISHKINA, O. 2024 Ultimate Rayleigh–Bénard turbulence. *Rev. Mod. Phys.* **96** (3), 035001.

LOHSE, D. & XIA, K.Q. 2010 Small-scale properties of turbulent Rayleigh–Bénard convection. *Annu. Rev. Fluid Mech.* **42**, 335–364.

MAGNAUDET, J. & EAMES, I. 2000 The motion of high-Reynolds-number bubbles in inhomogeneous flows. *Annu. Rev. Fluid Mech.* **32**, 659–708.

MAGNAUDET, J. & MERCIER, M.J. 2020 Particles, drops, and bubbles moving across sharp interfaces and stratified layers. *Annu. Rev. Fluid Mech.* **52**, 61–91.

MATHAI, V., LOHSE, D. & SUN, C. 2020 Bubbly and buoyant particle-laden turbulent flows. *Annu. Rev. Condens. Matter Phys.* **11**, 529–559.

MENG, X.H., WU, J.Z., CHONG, K.L. & ZHOU, Q. 2026 Thermal and kinetic energy dissipation rates in vertical convection over rough sidewalls. *Phys. Fluids* **38**, 035137.

MIALDUN, A., RYZHKOV, I.I., MELNIKOV, D.E. & SHEVTSOVA, V. 2008 Experimental evidence of thermal vibrational convection in a nonuniformly heated fluid in a reduced gravity environment. *Phys. Rev. Lett.* **101** (8), 084501.

MUKHERJEE, S., SAFDARI, A., SHARDT, O., KENJERES, S. & VAN DEN AKKER, H.E.A. 2019 Droplet–turbulence interactions and quasi-equilibrium dynamics in turbulent emulsions. *J. Fluid Mech.* **878**, 221–276.

NATAF, H.C., MORENO, S. & CARDIN, P. 1988 What is responsible for thermal coupling in layered convection? *J. Phys. (Paris)* **49**, 1707–1714.

NI, R. 2024 Deformation and breakup of bubbles and drops in turbulence. *Annu. Rev. Fluid Mech.* **56** (1), 319–347.

PELUSI, F., SBRAGAGLIA, M., BENZI, R., SCAGLIARINI, A., BERNASCHI, M. & SUCCI, S. 2021 Rayleigh–Bénard convection of a model emulsion: anomalous heat-flux fluctuations and finite-size droplet effects. *Soft Matt.* **17**, 3709–3721.

PELUSI, F., SCAGLIARINI, A., SBRAGAGLIA, M., BERNASCHI, M. & BENZI, R. 2025*a* Dynamical regimes of thermally convective emulsions. *Phys. Rev. E* **111**, 065401.

PELUSI, F., SCAGLIARINI, A., SBRAGAGLIA, M., BERNASCHI, M. & BENZI, R. 2025*b* Role of interfacial stabilization in the Rayleigh-Bénard convection of liquid-liquid dispersions. *Phys. Rev. Fluids* **10**, 124305.

PERAZZO, A., PREZIOSI, V. & GUIDO, S. 2015 Phase inversion emulsification: current understanding and applications. *Adv. Colloid Interface Sci.* **222**, 581–599.

PERLEKAR, P., BIFERALE, L., SBRAGAGLIA, M., SRIVASTAVA, S. & TOSCHI, F. 2012 Droplet size distribution in homogeneous isotropic turbulence. *Phys. Fluids* **24** (6), 065101.

PETERS, F. & ARABALI, D. 2013 Interfacial tension between oil and water measured with a modified contour method. *Colloids Surf. A* **426**, 1–5.

VAN DER POEL, E.P., STEVENS, R.J.A.M. & LOHSE, D. 2013 Comparison between two- and three-dimensional Rayleigh–Bénard convection. *J. Fluid Mech.* **736**, 177–194.

POPINET, S. 2009 An accurate adaptive solver for surface-tension-driven interfacial flows. *J. Comput. Phys.* **228** (16), 5838–5866.

POPINET, S. 2013 Basilisk C. Available at: http://basilisk.fr/. Open-source software, accessed 13 July 2026.

POPINET, S. 2015 A quadtree-adaptive multigrid solver for the Serre-Green-Naghdi equations. *J. Comput. Phys.* **302**, 336–358.

https://doi.org/10.1017/jfm.2026.12243

PRAKASH, A. & KOSTER, J.N. 1994 Convection in multiple layers of immiscible liquids in a shallow cavity. I. steady natural convection. *Intl J. Multiphase Flow* **20** (2), 383–396.
QI, H., ZHAO, C., FAN, Y., DU, Y., MATHAI, V. & SUN, C. 2026 Active biphasic heat transfer enhancement in vertical natural convection. *Intl J. Multiphase Flow* **194**, 105396.
RAVERA, F., DZIZA, K., SANTINI, E., CRISTOFOLINI, L. & LIGGIERI, L. 2021 Emulsification and emulsion stability: the role of the interfacial properties. *Adv. Colloid Interface Sci.* **288**, 102344.
ROSTI, M.E., GE, Z., JAIN, S.S., DODD, M.S. & BRANDT, L. 2019 Droplets in homogeneous shear turbulence. *J. Fluid Mech.* **876**, 962–984.
SAVINO, R., MONTI, R. & PICCIRILLO, M. 1998 Thermovibrational convection in a fluid cell. *Comput. Fluids* **27** (8), 923–939.
SHEVTSOVA, V., RYZHKOV, I.I., MELNIKOV, D.E., GAPONENKO, Y.A. & MIALDUN, A. 2010 Experimental and theoretical study of vibration-induced thermal convection in low gravity. *J. Fluid Mech.* **648**, 53–82.
SIGGIA, E.D. 1994 High Rayleigh number convection. *Annu. Rev. Fluid Mech.* **26** (1), 137–168.
SOLIGO, G., ROCCON, A. & SOLDATI, A. 2019 Breakage, coalescence and size distribution of surfactant-laden droplets in turbulent flow. *J. Fluid Mech.* **881**, 244–282.
SOMEYA, S. & MUNAKATA, T. 2005 Measurement of the interface tension of immiscible liquids interface. *J. Cryst. Growth* **275** (1–2), e343–e348.
SU, J., WANG, C., ZHANG, Y.B., XU, F., WANG, J. & SUN, C. 2024*a* Turbulence modulation in liquid–liquid two-phase Taylor–Couette turbulence. *J. Fluid Mech.* **999**, A98.
SU, J., YI, L., ZHAO, B., WANG, C., XU, F., WANG, J. & SUN, C. 2024*b* Numerical study on the mechanism of drag modulation by dispersed drops in two-phase Taylor–Couette turbulence. *J. Fluid Mech.* **984**, R3.
SU, J., ZHANG, Y.B., WANG, C., YI, L., XU, F., FAN, Y., WANG, J. & SUN, C. 2025 How interfacial tension enhances drag in turbulent Taylor–Couette flow with neutrally buoyant and equally viscous droplets. *J. Fluid Mech.* **1002**, A2.
SUN, C. & TOSCHI, F. 2027 The physics of flowing dense emulsions. *Annu. Rev. Fluid Mech.* **59**, 6 1–6 28.
SUN, Y., XIE, Y.-C., XIE, J.-X., ZHONG, J.-Q., ZHANG, J. & XIA, K.-Q. 2024 Model for the dynamics of the large-scale circulations in two-layer turbulent convection. *Phys. Rev. Fluids* **9**, 033501.
WANG, B.F., ZHOU, Q. & SUN, C. 2020*a* Vibration-induced boundary-layer destabilization achieves massive heat transport enhancement. *Sci. Adv.* **6** (21), eaaz8239.
WANG, M., CHEN, X.-Y., WANG, W. & WEI, P. 2024 Heat transport and flow structure in thermal convection with two liquid layers. *J. Fluid Mech.* **978**, A4.
WANG, Z., MATHAI, V. & SUN, C. 2019 Self-sustained biphasic catalytic particle turbulence. *Nat. Commun.* **10**, 3333.
WANG, Z., MATHAI, V. & SUN, C. 2020*b* Experimental study of the heat transfer properties of self-sustained biphasic thermally driven turbulence. *Intl J. Heat Mass Transfer* **152**, 119515.
WU, J.Z., WANG, B.F., CHONG, K.L., DONG, Y.H., SUN, C. & ZHOU, Q. 2022 Vibration-induced anti-gravity tames thermal turbulence at high Rayleigh numbers. *J. Fluid Mech.* **951**, A13.
XIA, K.-Q., CHONG, K.L., DING, G.-Y. & ZHANG, L. 2025 Some fundamental issues in buoyancy-driven flows with implications for geophysical and astrophysical systems. *Acta Mechanica Sin.* **41** (1), 324287.
XIA, K.Q., HUANG, S.D., XIE, Y.C. & ZHANG, L. 2023 Tuning heat transport via coherent structure manipulation: recent advances in thermal turbulence. *Natl Sci. Rev.* **10** (6), nwad012.
XIE, Y.-C. & XIA, K.-Q. 2013 Dynamics and flow coupling in two-layer turbulent thermal convection. *J. Fluid Mech.* **728**, R1.
YI, L., GIROTTO, I., TOSCHI, F. & SUN, C. 2024 Divergence of critical fluctuations on approaching catastrophic phase inversion in turbulent emulsions. *Phys. Rev. Lett.* **133**, 134001.
YI, L., TOSCHI, F. & SUN, C. 2021 Global and local statistics in turbulent emulsions. *J. Fluid Mech.* **912**, A13.
YI, L., WANG, C., HUISMAN, S.G. & SUN, C. 2023 Recent developments of turbulent emulsions in Taylor–Couette flow. *Phil. Trans. R. Soc. A* **381** (2243), 20220129.
YI, L., WANG, C., VAN VUREN, T., LOHSE, D., RISSO, F., TOSCHI, F. & SUN, C. 2022 Physical mechanisms for droplet size and effective viscosity asymmetries in turbulent emulsions. *J. Fluid Mech.* **951**, A39.
YU, X., HENDRICKSON, K. & YUE, D.K.P. 2020 Scale separation and dependence of entrainment bubble-size distribution in free-surface turbulence. *J. Fluid Mech.* **885**, R2.
YUGE, T. & HAGIWARA, Y. 2004 The modifications of near-wall turbulence structure and heat transfer by immiscible droplets in turbulent liquid–liquid two-phase flow. *Intl J. Heat Fluid Flow* **25** (3), 471–480.
ZHANG, Y., ZHOU, Q. & SUN, C. 2017 Statistics of kinetic and thermal energy dissipation rates in two-dimensional turbulent Rayleigh–Bénard convection. *J. Fluid Mech.* **814**, 165–184.
ZHAO, X.-Z., QIU, C., ZHOU, S.-Q., LI, Y.-Z., XI, H.-D. & XIA, K.-Q. 2024 Heat transport in three-layer turbulent thermal convection. *Phys. Rev. Fluids* **9**, 073501.

https://doi.org/10.1017/jfm.2026.12243